

UNIVERSITAT DE BARCELONA  
DEPARTAMENT D'ASTRONOMIA I METEOROLOGIA  
MASTER IN ASTROPHYSICS, PARTICLE PHYSICS AND COSMOLOGY



# LOW FREQUENCY RADIO OBSERVATIONS OF GAMMA-RAY BINARIES

BENITO MARCOTE MARTIN

MASTER THESIS

Under the supervision of:  
**Dr. Josep M. Paredes Poy**

Barcelona, September 2012



# Low Frequency Radio Observations of Gamma-Ray Binaries

BENITO MARCOTE MARTIN

*Universitat de Barcelona*

## ABSTRACT

In this work we present a low frequency radio study of one of the known gamma-ray binaries, LS 5039. This source has been studied from its beginnings by the research group on *High Energy Astrophysics* of the University of Barcelona and has been observed at all the possible energies, from radio to very high energy gamma-rays. With the new generation of low frequency radio observatories that are starting to operate, as LOFAR, we are able to improve the knowledge of the gamma-ray binaries at low frequencies, a region which remains poorly explored up to now. For that reason, we focus our efforts on an intensive study of the gamma-ray binaries at low frequencies, improving our knowledge about them.

The first chapter of this master thesis is a general background explanation about gamma-ray binaries and their radio emission. In this chapter we also explain briefly the X-ray binaries, their differences with the gamma-ray binaries, and the proposed scenarios to explain the emission for the gamma-ray binaries.

The second chapter describes the gamma-ray binary LS 5039. Its orbital parameters, its X-ray, high-energy and very high-energy gamma-ray emission are discussed and also the behaviour of its radio emission at different frequencies that is known up to now.

The third chapter discusses the radio observatories which have been used to perform this master thesis: LOFAR, VLA and GMRT. Since at low frequencies the radio data reduction is slightly different than the classical reduction at high frequencies, we also describe the different ways to manage a calibration of radio data.

Finally, last chapters show the results obtained for LS 5039 with the performed observations and the conclusions we can extract from this information comparing it with the published data.



---

# Contents

---

<b>1</b>	<b>Introduction</b>	<b>7</b>
1.1	High-Energy Astrophysics . . . . .	7
1.2	Binaries displaying Gamma-Ray Emission . . . . .	8
1.2.1	X-ray Binaries . . . . .	8
1.2.2	Gamma-Ray Binaries . . . . .	9
1.3	Gamma-ray Binary System Scenarios . . . . .	10
1.3.1	Microquasar scenario . . . . .	10
1.3.2	Binary pulsar or young non-accreting pulsar scenario . . . . .	10
1.4	Radio emission from Gamma-Ray Binaries . . . . .	11
1.4.1	Synchrotron emission . . . . .	11
1.4.2	Synchrotron self-absorption . . . . .	12
<b>2</b>	<b>The Gamma-Ray Binary LS 5039</b>	<b>13</b>
2.1	Radio emission of LS 5039 . . . . .	14
<b>3</b>	<b>Radio Observatories and Data Reduction</b>	<b>15</b>
3.1	The Very Large Array (VLA) . . . . .	15
3.2	The Giant Metrewave Radio Telescope (GMRT) . . . . .	16
3.3	The Low Frequency Array (LOFAR) . . . . .	16
3.4	Interferometric Radio Data Calibration . . . . .	17
3.4.1	Phase-referencing Calibration . . . . .	18
3.4.2	Low Frequency Calibration . . . . .	19
<b>4</b>	<b>Observations and Results</b>	<b>21</b>
4.1	LOFAR observation . . . . .	22
4.2	Low Frequency VLA Observations . . . . .	23
4.3	VLA monitoring . . . . .	26
4.4	Low frequency variability of LS 5039 . . . . .	27
<b>5</b>	<b>Conclusions</b>	<b>31</b>
	<b>Bibliography</b>	<b>33</b>



## 1.1. High-Energy Astrophysics

In the last decades, High-Energy Astrophysics has emerged as one of the most interesting topics in physics. This young research field, in which we need to combine the high energy particle physics with the classical astrophysics, is in continuously development. Therefore, new ideas and new theoretical perspectives are taken into account in order to maintain a consistent model which explains the observations of high energy sources.

High-Energy Astrophysics is the study of those astrophysical systems displaying X-ray or gamma-ray emission, but also those which emits neutrinos or cosmic rays. As the most energetic emission can not be explained by hot matter (this explanation would require so high temperatures to be physically possible), it necessarily involves non-thermal processes. These processes are related to relativistic particles accelerated on energetic scenarios where a strong interaction with the environment (magnetic field, radiation and cold gas) takes place. Commonly, we are talking about two energy ranges for the gamma-rays: High-Energy (HE), 100 MeV–100 GeV, and Very High Energy (VHE),  $\gtrsim 100$  GeV. Hence we can talk about sources with HE emission or VHE emission.

As the High-Energy Astrophysics requires the observation of X-ray and gamma-ray photons, and these photons can not reach the Earth surface, this kind of astrophysics has been closely linked to the development of X-ray and gamma-ray observatories which could detect this emission from astrophysical sources. Focusing on the gamma-rays, for the 0.1–100 GeV range we have had the Energetic Gamma Ray Experiment Telescope (EGRET) on board on the *Compton Gamma Ray Observatory* satellite (*CGRO*), in operation from 1991 to 2000. Nowadays, we have the last generation of space telescopes: *Fermi* and *AGILE*. For the photons with a higher energy, the reduced number of photons which comes to us makes impractical their observation with this kind of satellites. Therefore, a new way to observe the most energetic gamma-rays has been carried out by ground detectors which observe either direct air shower particle or atmospheric Cherenkov radiation. Three Cherenkov observatories are available at the present: High Energy Stereoscopic System (H.E.S.S.), the Major Atmospheric Gamma-ray Imaging Cherenkov telescopes (MAGIC) and the Very Energetic Radiation Imaging Telescope Array System (VERITAS). There was also a direct detector of the air shower particle, MILAGRO. Figure 1.1 shows a map with the known sources emitting VHE. The complete population of sources which are able to produce a High Energy emission ( $\gtrsim 100$  MeV) can be described only by a few categories of Galactic and extragalactic systems: Supernova Remnants (SNRs), Pulsar Wind Nebulae (PWNe), open clusters, Active Galactic Nuclei (AGNs) or even unidentified sources (gamma-ray sources without a known counterpart), microquasars, Gamma Ray Bursts (GRBs) or binary systems with a young high-mass star.

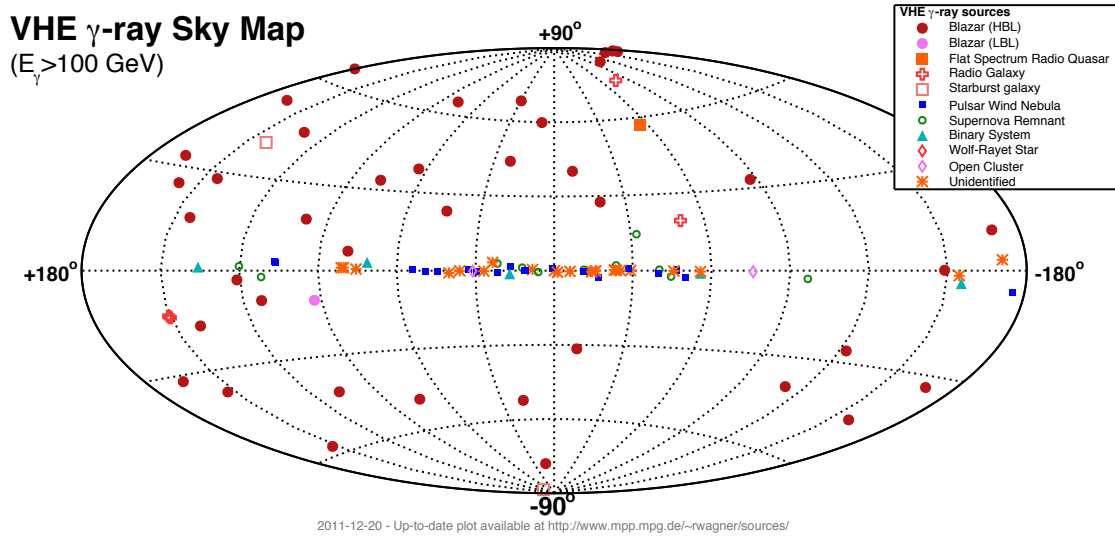


**Figure 1.1.** All-sky map of sources detected above 100 GeV as of November 20, 2011. Image courtesy of Robert Wagner. Up-to-date plot available at <http://www.mppmu.mpg.de/~rwagner/sources>.

## 1.2. Binaries displaying Gamma-Ray Emission

There are some binary systems detected as high energy and/or very high energy gamma-ray emitters. These systems display emission from radio wavelengths to gamma-rays and are formed by a normal star (often called the donor star) and a compact object around it, which can be either a neutron star or a black hole. The interaction between both bodies causes the broadband emission at X-rays and gamma-rays.

At this state-of-the art, we are able to identify two different types of binary systems displaying gamma-ray emission: the X-ray binaries and the gamma-ray binaries. A different behaviour is displayed in each one. Although we are just focusing on the gamma-ray binaries, for a better understanding of these systems we will describe the both types of binary systems which display gamma-ray emission.

### 1.2.1. X-ray Binaries

The X-ray binaries are a type of binary systems which are known since the sixties, with the discovery of Scorpius X-1 by [Giacconi et al. \(1962\)](#). They are characterized by displaying a strong luminosity in X-rays (its non-thermal spectral energy distribution (SED) is clearly dominated by the X-ray emission; see [Fender et al. 2004](#) for a recent review).

Although there are two main types of X-ray binaries depending on the mass of the optically visible star: Low-Mass X-Ray Binaries (LMXBs) and High-Mass X-Ray Binaries (HMXBs), the process of X-ray emission is basically the same on both of them. An accretion process, with a transfer of mass from the visible star to the compact object, heats the mass as a consequence of friction. This heating is the responsible of the strong



X-ray thermal emission. The differences between both types of X-ray binaries involve differences in the process of accretion mass from the donor star to the compact object. For a full description of these sources, see [Lewin & van der Klis \(2006\)](#).

### Low-Mass X-Ray Binaries

The LMXBs are binary stars where there are a low-mass star, which can be a main-sequence star, a white dwarf or a red giant, and a compact object (either a neutron star or a black hole). The donor star is less massive than the compact object and fills its Roche lobe. Therefore, this star transfers mass to the compact object, forming an accretion disk around the compact object.

### High-Mass X-Ray Binaries

The HMXBs are binary systems where the donor star is a massive star (an O or B star). These stars show more powerful winds than the less massive stars, with a larger mass-loss rate due to this wind. For this reason, the accretion of mass by the compact object is given by a capture of the wind ejected by the star, rather than a Roche-lobe overflow. A recent review on HMXBs with a focus on Be X-ray binaries can be found in [Reig \(2011\)](#). One of the most famous high-mass X-ray binary is Cygnus X-1, which was identified as the first black hole candidate.

We emphasized that, although there are X-ray binaries showing gamma-ray emission, the behaviour of these sources is determined by displaying a non-thermal spectral energy distribution (SED) clearly dominated by the X-ray emission. The gamma-ray emission of X-ray binaries is occasional. Up to now, two X-ray binaries are known to be gamma-ray emitters: Cygnus X-3, clearly detected by both *Fermi* ([Fermi LAT Collaboration et al. 2009](#)) and *AGILE* ([Tavani et al. 2009](#)), and Cygnus X-1, possibly detected by *AGILE* ([Sabatini et al. 2010](#)) and *MAGIC* ([Albert et al. 2007](#)).

#### 1.2.2. Gamma-Ray Binaries

The gamma-ray binaries are another type of binary systems which display gamma-ray emission. In opposition to X-ray binaries, which have been exhaustively studied along the last fifty years, the gamma-ray binaries are emerging as a new and different type of binary systems. Only in the last years their main properties have been unveiled.

These systems show a non-thermal SED clearly dominated by the gamma-ray emission (MeV-GeV) and display an emission from radio to VHE gamma-rays. Because of displaying a SED dominated by the gamma-ray emission, instead of by the X-ray emission, we refer to these sources as gamma-ray binaries. This definition is also physically consistent with the fact that the nature of these systems points out to be similar between them, but different from the X-ray binaries emitting gamma rays. For example, contrary to the X-ray binaries, which display different states along the time, the X-ray emission from gamma-ray binaries does not show signatures of an accretion disk and their emission is always modulated by the orbital period of the binary system and does not show changes between different states.

There are only five known sources showing the mentioned properties (Moldón 2012): PSR B1259–63, LS 5039, LS I +61 303, HESS J0632+057 and 1FGL J1018.6–5856, also detected as TeV emitters, and other binary system proposed to be a gamma-ray binary: AGL J2241+4454 (Williams et al. 2010). All of these systems consist of a luminous early-type star (O or B spectral type) and a compact object (a neutron star or a black hole, being the nature of this companion unidentified in most of the cases). As their emission covers all the electromagnetic spectrum, from radio wavelength to gamma-rays, we can observe these binaries with radio antennas, optical telescopes, X-ray or gamma-ray space telescopes or Cherenkov telescopes.

### 1.3. Gamma-ray Binary System Scenarios

Two main scenarios have been proposed to explain the emission of gamma-ray binaries: the *microquasar* and the *binary pulsar scenario* (often called as the young non-accreting pulsar scenario). Both scenarios provide a natural frame to explain the emission along all the electromagnetic spectrum.

Although these two scenarios give us two different description for the observed emission in gamma-ray binaries, the involved radiation mechanisms are basically the same in both of them: a population of high energy accelerated electrons displaying fundamental interactions (like synchrotron, inverse Compton or Bremsstrahlung emission).

#### 1.3.1. Microquasar scenario

The microquasar scenario has already been described briefly when we have talked about X-ray binaries: on these systems the compact object accretes matter from the star forming an accretion disk and in certain states a relativistic jet.

The presence of the accretion disk produces the extremely bright emission in X-rays, characterising the observed SED typical for the X-rays binaries. The HE emission is produced by the scattering of ultraviolet (UV) photons emitted by the star due to the relativistic electrons located in the jet. A deeper description of this scenario can be found in Bosch-Ramon & Khangulyan (2009).

This scenario comes as an analogy of the extragalactic quasars, because both systems are morphologically and physically equivalent from many points of view (only a scaling factor is needed to distinguish both of them). Whereas the HE emission comes from the interaction between the particles within the jets and the vicinity of the compact object, the radio emission emerges from the relativistic jets.

#### 1.3.2. Binary pulsar or young non-accreting pulsar scenario

The other proposed scenario is based on a young non-accreting pulsar as compact object. The pulsar provides an intense and relativistic pair plasma wind which produces a strong shock between it and the stellar wind of the massive companion star. On this shock the particles are accelerated up to relativistic velocities, radiating the HE and VHE emission.

Maraschi & Treves (1981) originally proposed this scenario in order to explain the non-thermal emission of LS I +61 303. Improvements of this scenario have been made by

Tavani & Arons (1997), Kirk et al. (1999) or Dubus (2006).

The radio emission from this scenario is the result of synchrotron radiation emitted along the pulsar nebula. The shocked wind flows away from the binary system on a straight direction, forming a cometary tail at larger scales. The direction of this tail will change with the orbital motion, describing a spiral which can be detected at radio wavelengths.

## 1.4. Radio emission from Gamma-Ray Binaries

We have talked about the HE or VHE emission of gamma-ray binaries, although we are going to focus only in their radio emission. This discussion was important because the radio emission is strongly related with the gamma-ray emission, and the better we understand this last emission the better we will understand the radio emission.

At low and very low frequencies the thermal emission is completely irrelevant and we have three main emission processes: the synchrotron emission, the inverse Compton, and the Bremsstrahlung. At frequencies  $\ll 1$  GHz, the synchrotron emission clearly dominates the emission of the source. For gamma-ray binaries we expect to observe synchrotron radio emission from the low-energy electrons at meter wavelengths. In the binary pulsar scenario this emission would be located in a region farther away from the binary system than at higher frequencies (at  $\sim$ GHz frequencies it happens at mas scales). As these electrons should remain unaffected either by inverse Compton or synchrotron cooling (Durant et al. 2011), we would expect to see synchrotron radio emission at arcsec–arcmin scales without variability along the orbit (Bosch-Ramon & Barkov 2011). However, this emission has remained unobserved due to the very poor resolution and sensitivity of the previous radio observatories at these very low-frequencies. Only with the new generation of low frequency observatories we will be able to observe this emission.

### 1.4.1. Synchrotron emission

Synchrotron emission is the radiation emitted by a relativistic charged particle accelerated in a magnetic field  $\vec{B}$ . The charged particle will describe a spiral around the direction of the magnetic field lines owing the Lorentz forces. As a consequence of this acceleration, the particle radiates at frequencies close to a characteristic frequency

$$\nu_c = \frac{3}{4\pi} \frac{eB \sin \phi}{m_e c} \gamma^2 \quad (1.1)$$

where  $B$  is the intensity of the magnetic field,  $\phi$  is the angle between the electron velocity and the magnetic field direction,  $\gamma$  is the Lorentz factor of the particle,  $m_e$  and  $e$  are the mass and charge of the electron and  $c$  is the speed of light. But the emission is radiated by the power function (Romero & Paredes 2011)

$$P(\gamma, \nu, \phi) = \frac{\sqrt{3}e^3 B \sin \phi}{hm_e c^2} \frac{\nu}{\nu_c} \int_{\nu/\nu_c}^{\infty} K_{5/3}(\xi) d\xi \quad (1.2)$$

where  $K_{5/3}$  is the Bessel function of second kind.

For a particle distribution, emitted isotropically and dependent of the energy by a power-law with index  $p$ , we get

$$P(\nu) = a(p) \frac{(4\pi)^2 K_0 e^3 B^{\frac{p+1}{2}}}{hmc^2} \left( \frac{3e}{4\pi m^3 c^5} \right)^{\frac{p-1}{2}} \nu^{-\frac{p-1}{2}} \quad (1.3)$$

with  $K_0$  a constant about the injection of particles, and

$$a(p) = \frac{2^{\frac{1}{2}(p-1)} \sqrt{3} \Gamma\left(\frac{3p-1}{12}\right) \Gamma\left(\frac{3p+19}{12}\right) \Gamma\left(\frac{p+5}{4}\right)}{8\sqrt{\pi}(p+1)\Gamma\left(\frac{p+7}{4}\right)} \quad (1.4)$$

Therefore, the synchrotron emission is displayed as a power-law with a spectral index  $\alpha$ :

$$P(\nu) \propto \nu^\alpha \quad (1.5)$$

For gamma-ray binaries, the typical non-thermal synchrotron radio emission is of the order of 0.1–100 mJy<sup>1</sup> and it usually shows a negative spectral index  $\alpha$  from  $-0.5$  to  $0$  for the  $\sim$  GHz frequencies.

### 1.4.2. Synchrotron self-absorption

At lower frequencies, some binaries show a cut-off produced by synchrotron self-absorption. The behaviour for the gamma-ray binaries is unknown. For LS I +61 303 there are no evidences of that cut-off for frequencies  $> 230$  MHz (Pandey et al. 2007). However, for LS 5039 there could be a variable behaviour, with a cut-off changing along the time (see §2.1).

This self-absorption is produced by the absorption of the radiation by the own electrons of the medium. The absorption coefficient is (Romero & Paredes 2011)

$$k_\nu = A\nu^{-\frac{1}{2}(p+4)} \quad (1.6)$$

where

$$A = \frac{\sqrt{3}e^3}{16\pi m} \left( \frac{3e}{4\pi m^3 c^5} \right)^{\frac{p}{2}} \sqrt{2\pi c} K_0 B^{(p+2)/2} \frac{\Gamma\left(\frac{3p+2}{12}\right) \Gamma\left(\frac{3p+22}{12}\right) \Gamma\left(\frac{p+6}{4}\right)}{\Gamma\left(\frac{p+8}{4}\right)} \quad (1.7)$$

Therefore, the radiated intensity is

$$I(\nu) = \frac{P(\nu)}{k_\nu} (1 - e^{-k_\nu \ell}) \quad (1.8)$$

where  $\ell$  is the linear dimension of the synchrotron source.

---

<sup>1</sup>The Jansky (Jy) is a typical unit for flux densities, defined as  $1 \text{ Jy} = 10^{-26} \text{ W m}^{-2} \text{ Hz}^{-1}$ .

# The Gamma-Ray Binary LS 5039

LS 5039 is a binary system with a young O6.5 star with a photometric visual magnitude of 11.3. Its position in J2000 coordinates in the epoch MJD 53797.064 is (Moldón et al. 2012a)

$$\alpha = 18^{\text{h}} 26^{\text{m}} 15.0593^{\text{s}} \quad \delta = -14^{\circ} 50' 54.301''$$

LS 5039 is known to be optically stable within 0.1 mag over the years and 0.002 mag on orbital timescales (Sarty et al. 2011). No pulsations have been found neither in radio (McSwain et al. 2011) nor in X-rays (Rea et al. 2011) and the orbital parameters could not determine if the companion is a black hole or a neutron star (Casares et al. 2005). See Table 2.1 for the more important parameters of the binary system. The detection

Magnitude	Parameter	Value
$P_{\text{orb}}$	Orbital period (days)	$3.90603 \pm 0.00017$
$T_0$	Periastron passage (MJD)	$51942.59 \pm 0.10$
$e$	Eccentricity	$0.35 \pm 0.04$
$\omega$	Argument of periastron (degrees)	$226 \pm 3$
$\gamma$	Systemic radial velocity ( $\text{km s}^{-1}$ )	$17.2 \pm 0.7$
$a_1 \sin i$	Projected semi-major axis ( $R_{\odot}$ )	$1.82 \pm 0.10$
$f(M)$	Mass function ( $M_{\odot}$ )	$0.0053 \pm 0.0009$
$v \sin i$	Projected rotational velocity ( $\text{km s}^{-1}$ )	$113 \pm 8$
$d$	System distance (kpc)	$2.5 \pm 0.5$
$M_*$	Compact object mass ( $M_{\odot}$ )	$1.49 < M < 10$
$M_X$	Stellar mass ( $M_{\odot}$ )	$22.9^{+3.4}_{-2.9}$
$R_*$	Stellar radius ( $R_{\odot}$ )	$9.3^{+0.7}_{-0.6}$
$L_*$	Stellar luminosity ( $\text{erg s}^{-1}$ )	$7 \times 10^{38}$
$\dot{m}$	Stellar mass loss rate ( $M_{\odot} \text{ yr}^{-1}$ )	$7 \times 10^{-7}$
$T_*$	Star temperature (K)	$(3.9 \pm 0.1) \times 10^4$

**Table 2.1.** Orbital parameters of the binary system LS 5039 and estimated stellar properties from Casares et al. (2005).

of LS 5039 as a high energy emitter was made by Paredes et al. (2000), associating an EGRET gamma-ray source with the LS 5039. HESS detected the binary system in the range 0.1–4 TeV (Aharonian et al. 2005) and variability at TeV energies along the orbital period was reported by Aharonian et al. (2006).

This source was firstly observed in X-rays by the ROSAT satellite (Motch et al. 1997),

and a flux modulation correlated with the orbital period was also detected (Bosch-Ramon et al. 2005, Kishishita et al. 2009).

In contrast with other gamma-ray binaries, like LS I +61 303 or PSR B1259–63, LS 5039 does not show a circumstellar disk which is thought to produce the observed variability along the orbit in the optical range.

## 2.1. Radio emission of LS 5039

In general terms, the radio emission of LS 5039 at  $\sim$  GHz frequencies is non-thermal, persistent, and variable. No strong radio outbursts or periodic variability have been detected.

Martí et al. (1998) conducted a multiwavelength study of LS 5039 using the VLA in its A configuration (see §3.1). The observations were taken in four different epochs, separated around one month, at wavelengths of 20 cm, 6 cm, 3.6 cm and 2.0 cm (1.4 GHz, 5 GHz, 8.5 GHz and 15 GHz, respectively). For this frequency range, the radio flux of the source is clearly non-thermal and can be described by

$$S_\nu[\text{mJy}] = (52 \pm 1) \nu[\text{GHz}]^{-0.46 \pm 0.01} \quad (2.1)$$

This emission is persistent with a variability below 30%.

With VLBA observations, Paredes et al. (2000) showed an asymmetrical bipolar extended emission on both sides of a bright core, and suggested that LS 5039 was a microquasar. Ribó et al. (2008) pointed out that a microquasar scenario can not easily explain the observed changes in the morphology of LS 5039. Finally, a periodic morphological variability has been observed at mas scales, clearly supporting the binary pulsar scenario (Moldón et al. 2012b).

At low frequencies, only three observations have been reported. Godambe et al. (2008) show, with one GMRT observation in 2008 simultaneously at 610 and 235 MHz, that the spectrum of LS 5039 is inverted (positive spectral index), indicating an optically thick radio spectrum with a turnover at  $\approx$ 1 GHz. However, Pandey et al. (2007) reported with two GMRT observations in 2003 and 2005, also at 610 and 235 MHz, that LS 5039 does not show any turnover for this range of frequencies, with compatible values between both observations. i.e. reporting a non variability of LS 5039 in these two epochs. Although the flux density values at 610 MHz for the three observations are compatible, at 235 MHz they demand a variability of  $\sim$  80 % in 3 years (from 2005 to 2008): from  $74.6 \pm 5.6$  mJy to  $17.0 \pm 1.1$  mJy. Therefore, a large variability at about year scales would happen in LS 5039 but only for the low frequencies.

---

CHAPTER 3

# Radio Observatories and Data Reduction

---

The results of this work have been obtained using the data of different radio observatories. As they exhibit different properties and there are different ways to work with their data, we describe briefly all these observatories and how the radio data are usually reduced.

Before that, we consider helpful clarifying one definition concerning to the radio range. Although there is not a well-established classification and depends on research fields and capabilities, we normally talk of very-low frequencies for  $\lesssim 100$  MHz, low frequencies for the range 100 MHz–GHz and high frequencies for  $\gtrsim$  GHz. However, talking about radio data calibration, sometimes the low frequencies are referred to frequencies  $\lesssim 300$  MHz and high frequencies to larger than it. This distinction is made because at 300 MHz the calibration approach changes and we need to use different techniques. Even, as we will see for the LOFAR observatory, the high band, or high frequencies, definition is sometimes used for the antennas which observe at 110–250 MHz; and low band, or low frequencies, for 10–80 MHz.

## 3.1. The Very Large Array (VLA)

The Very Large Array (VLA)<sup>1</sup>, recently renamed as the Karl G. Jansky Very Large Array (JVLA) and also known as Expanded Very Large Array (EVLA) after its last upgrade in 2009, consists of 27 25-meter diameter antennas located on the Plains of San Agustin in New Mexico (USA). It is managed by the USA National Radio Astronomy Observatory (NRAO). The JVLA antennas are distributed in a Y configuration with four principal configurations A, B, C and D, in which the maximum antenna separations are 36.4 km, 11.1 km, 3.4 km and 1.0 km, respectively. The current configuration changes every six months and mixed configuration (BC, AB, etc) are also possible.

The JVLA operates at any frequency between 1.0 and 50 GHz (30 cm and 6 mm wavelengths), with up to 8 GHz bandwidth per polarization and 64 sub-band pairs. The point-source sensitivity is between 2 and 6  $\mu$ Jy after one hour of observation. From 1998 to 2008 the VLA also had detectors for low frequency observations: at 74 MHz and 330 MHz (4 m and 90 cm). These detectors were removed from the current setup due to technical problems and will be reintroduced with an important upgrade in the coming years.

---

<sup>1</sup><https://science.nrao.edu/facilities/evla/>



## 3.2. The Giant Metrewave Radio Telescope (GMRT)

The Giant Metrewave Radio Telescope (GMRT)<sup>1</sup> is an observatory located near Pune, in India. GMRT consists of 30 45-meter diameter dishes spread over distances of up to 25 km. It is operated by the National Centre for Radio Astrophysics, a part of the Tata Institute of Fundamental Research.

Fourteen of the dishes are located more or less randomly in a compact central array in a region of  $\sim 1 \text{ km}^2$ . The remaining dishes are spread out along 3 arms describing approximately a Y-shaped configuration. GMRT operates in six frequency bands around 50, 153, 233, 325, 610 and 1420 MHz, with a bandwidth of 32 MHz and a resolution from 60 arcsec to 2 arcsec, for the lowest to the highest frequency.

## 3.3. The Low Frequency Array (LOFAR)

The Low Frequency Array (LOFAR)<sup>2</sup> is a digital radio interferometer with stations in The Netherlands, France, Germany, Sweden and the United Kingdom which will observe continuously a large fraction of the northern hemisphere (see [Heald et al. 2011](#) for a recent update of the LOFAR status). LOFAR detects photons in the frequency range 30–240 MHz, which has never been explored by any large-scale interferometer before. Operating in this new frequency window LOFAR promises to revolutionize wide ranging areas of astrophysics.

The LOFAR radio telescope consists of many new generation low-cost antennas, distributed in 24 core, 18 remote and 8 international stations (more stations could be added in the future), with baselines from 100 m to 1500 km. There are two types of antennas: the Low Band Antennas (LBAs), observing at 30–80 MHz and the High Band Antennas (HBAs), designed to operate in the range 120–240 MHz (with three observing bands: 110–190, 170–230 and 210–250 MHz). In the final configuration, LOFAR will reach a resolution of 0.65 arcsec and a sensitivity of  $10 \text{ mJy beam}^{-1}$  in one hour of observation with the LBA and a resolution of 0.2 arcsec and a sensitivity of  $0.3 \text{ mJy beam}^{-1}$ , in one hour of observation, with the HBA.

LOFAR started preliminary observations in 2008, and has conducted detailed commissioning observations in 2011 and 2012. In September 2012, LOFAR is starting regular proposal calls for observations to the worldwide community. The key science projects (KSPs) of LOFAR are: epoch of reionization, deep extragalactic surveys, transient sources, ultra high energy cosmic rays, solar science and space weather, and cosmic magnetism.

LOFAR brings some new ideas about how new generation low frequency radio observatories are being built that contrasts with the classical observatories like JVLA or GMRT:

- Instead of parabolic dish antennas, LOFAR uses low cost omni-directional dipole antennas with no moving parts. Every single antenna can observe approximately all the sky, and the interferometric process is done completely computationally.

---

<sup>1</sup><http://gmrt.ncra.tifr.res.in>

<sup>2</sup><http://www.lofar.org>



Therefore, we only have to choose in which region of the sky we wish to observe and hence to that direction we will correlate the signal from all the antennas (forming the beam of the equivalent antenna). Whereas with the classical antennas we need to point out the dishes in the direction we want to observe.

The advantage of these antennas lies in the larger field of view of the resulting image, and in the possibility to correlate the signal in different regions of the sky at the same time, observing different regions simultaneously. The low cost antennas also allow to increase the total number of antennas, promising a better covering of the observed region of the sky.

As disadvantage, the more simplicity of the antennas produces larger levels of noise and some antennas could produce bad signals during an observation.

- As a consequence of the previous point, the data volume generated for these observatories is extremely huge compared with the old ones. As an example, LOFAR generates  $\sim 1$  GB/s raw data. And for a beam forming observation, LOFAR will produce approximately up to 10 TB per hour of observation. This amount of data makes impractical to perform the data reduction in the computers we typically have in our office. For that reason, the LOFAR observations are calibrated by a Standard Imaging Pipeline that runs on the Central Processing Systems (CEP) of LOFAR (located in Groningen, The Netherlands).

These points are becoming common for the new generation of very low frequency observatories, as LOFAR, the Low Wavelength Array (LWA), the Murchison Widefield Array (MWA) or in the future the Square Kilometer Array (SKA).

### 3.4. Interferometric Radio Data Calibration

Reduction of radio observations is completely different of observations in other electromagnetic range, as in infrared, optical, ultraviolet, X-rays or gamma-rays. Although here we won't describe the interferometric basis (the interested reader can find all the details in [Taylor et al. 1999](#)), we will describe briefly the data reduction process.

The output of the correlated signal from the antennas is a complex number called *visibility*. It contains the information of the amplitude and the phase of the signal received for a couple of antennas (i. e. a given baseline), for a given time and frequency channel. These visibilities are the Fourier transform of the radio flux density distribution in the plane of the sky (or radio image). To recover the original radio image we have to make a Fourier transform of the observed visibilities, which do not cover all the Fourier space. Therefore, the more baselines we have, the better will be the Fourier transform, and thus the obtained radio image.

The problem with the observed sky is that this is the 'real' sky affected by many problems that must be corrected: problems with the receivers and the noise in the antenna signal, bad correlated phases, wrong amplitudes in the signal for some antennas, external and contaminating signals and so on. For this reason, the radio data must be corrected from these effects before obtaining the image of the sky. This process, the calibration

of the data, basically consists in four steps: the flagging, the calibration, the cleaning process, and the self-calibration.

- The *flagging* process consists in looking all the visibilities and removing all the bad data. This bad data can be due to external interferences observed by the antennas (usually called RFI: Radio Frequency Interferences), but also data taken from antennas which did not work properly.
- The *calibration* process is made after the flagging, when we already have good visibilities. We need to modify these visibilities, correcting their amplitudes to the real ones and the phases to be well-correlated between every couple of antennas.

This process depends a lot on the frequency at which we are working and in the longest baselines we are using: the calibration of low frequency data is different of the high frequency, and the data from compact observatories (like VLA with baselines up to  $\sim 40$  km) needs less corrections than the data from long baseline observatories like VLBI (with baselines up to  $\sim 10\,000$  km). Below we will discuss the different calibration styles as a function of the frequency.

- The *cleaning* process consists in recovering the observed sky from the dirty image we have obtained with the corrected visibilities. This dirty image is the image of the sky convolved with the antenna array pattern. For that, we need to deconvolve this image in order to recover the real image of the sky.
- Once we have an image, sometimes (always at low frequencies) a *self-calibration* of the data is done. This process uses a model for the sky made during the cleaning process in order to improve the amplitudes and phases of the data and get a better image. Self-calibration iteratively minimizes the differences between the observed data and predictions based on the model of the sky. This model is updated after each iteration, based on an analysis of the differences between predicted and observed visibilities.

### 3.4.1. Phase-referencing Calibration

The classical radio calibration for interferometric observations, known as phase-referencing technique, has been used for the last decades on radio astronomy and it is the useful technique for high frequency observations but also for low frequencies. Here we understand by high frequency the frequencies larger than 300 MHz.

In this technique, a bright compact reference source within a few degrees of the target source position is observed every few minutes along the observation, called the *phase calibrator*. This allows us to avoid differential atmospheric propagation effects determining the phase calibration from this source. That is, with the data of this source we are able to determine the evolution of the phases of the radio waves that are taken by the antennas and correlated later. Ideally the phase angle should be zero, indicating a good correlation between all the signals, but in reality they are not zero. With this bright source we can estimate their evolution along the observation and compensate this effect for our target source.

Another source with a known flux density (supposed to be constant in time) is also observed, the *flux calibrator*. Usually after the beginning and just before the end of the observation. As the flux of this source is known we can correct the flux we get for this source with our antennas by the real one, and translate this correction for the other sources, like the phase calibrator and the target source.

With this corrections we are able to guarantee a correct flux and a good image (with the phases well correlated) for our target source.

### 3.4.2. Low Frequency Calibration

In contrast with the above, for lower frequency observations (below 300 MHz), sometimes is used another type of calibration. At a low frequencies we have two factors that allow us to correct the data without the use of phase and amplitude calibrators. One, at these frequencies there are sources with a flux much larger than at higher frequencies (for example Cygnus A has a flux density of  $\sim 10\,000$  Jy at  $\sim 100$  MHz, whereas at  $\sim$  GHz frequencies its flux is  $\sim$  Jy). Second, the field of view of the antennas is inversely proportional to the frequency. For that reason this is larger at low frequencies than at high frequencies. Therefore, in an image we can detect several bright sources. Because of that, one option that is used by the LOFAR observatory but also by others like the LWA, is not to observe any calibrator, only the target source. As in that field we will have several bright sources, most of them without changes along the time, we can apply one model of the sky to that observation. Minimizing the differences between the results of the signal and the model, we will get a calibrated data set. One of the usefulness of this method is that all the observing time is spent in the target source, and we do not waste time in other sources and moving the antennas (or correlating in another direction of the sky during a fraction of the time).

This process is equivalent to the already-mentioned self-calibration, because as we do not have information about other reference sources to calibrate the data, we need a good model of the sky we are observing, which covers at least the primary beam of the antennas. During this process, first the brighter sources of the sky that are seen in the observation are used to correct the data for instrumental and ionospheric effects. Later, all the sources defined in the sky model are subtracted from the data, minimizing the differences between the observed data and the predictions based on the given model. After this “self-calibration”, the data set will be well calibrated, with equivalent results from a phase-referencing calibration.



---

## CHAPTER 4

# Observations and Results

---

Our objective is to characterize the behaviour of LS 5039 at low and very low frequencies, trying to detect the large scale structure which we expect to see according to the theoretical models (Durant et al. 2011) and clarify if LS 5039 shows variability at these frequencies. To do that, we have worked with archival data and new observations of LS 5039: two unpublished archival observations with the VLA which we have reduced and a new observation we have conducted with LOFAR.

The LOFAR observation, taken during its commissioning stage, allows us to determine the behaviour we can expect for the gamma-ray binaries like LS 5039 at this new frequency range (up to now there were no observations at  $\sim 100$  MHz with this sensitivity and angular resolution). We are also able to test the real capabilities which LOFAR will have when it will be opened to the community. This observation is a starting point for future researches with the LOFAR observatory. Existing observations of LS 5039 at low frequencies were searched in the observatory data archives. We found several (11) observations with the GMRT at 244 and 614 MHz (both frequencies observed simultaneously) and one observation at 157 MHz, all of them taken between 2004 and 2008. Only three of them have been published: two in Pandey et al. (2007) and one in Godambe et al. (2008). One low frequency VLA observation at 330 MHz was also carried out in 2006 (project code AM877) with unpublished results. We retrieved all these data to perform a long-term monitoring on the behaviour of LS 5039. Unfortunately, we have only been able to obtain results from the VLA data. For the GMRT observations we have not been able to perform a good calibration of the data. This will be done in the coming months, after a training in GMRT data reduction during a short stay in India. We will also reduce again the published GMRT data to obtain a coherent data set. At  $\sim$ GHz frequencies, we know that there is a small (below 30 %) variability. But a better understanding about if that variability has a periodic behaviour or not would help us to clarify the origin of the low frequency variability at 80 % level possibly detected on year timescales. For that point, we have reduced the data corresponding to a monitoring of LS 5039 performed with the VLA at higher frequencies during 2002 along several orbits. These data (project code AP444) also remained unpublished.

The data reduction of the VLA observations was done using the *Common Astronomy Software Applications package* (CASA), of the National Radio Astronomy Observatory (NRAO). Whereas the calibration of the LOFAR observation was done with the LOFAR Standard Imaging Pipeline, and the imaging process with the CASA software.

## 4.1. LOFAR observation

During the commissioning stage of LOFAR, we obtained one deep observation of LS 5039. It was made on October 1, 2011, when the post-periastron phase of LS 5039 was 0.67–0.73. The observing time on the source was 6 hours. This observation was made with the High Band Antennas (HBAs) in the range of 110–160 MHz with 244 subbands. 23 core stations (baselines up to 3 km) and 9 remote stations (up to 80 km) were used. The elevation of the source during the observation was less than 20 degrees and no calibrators were required during the observation.

### Data Reduction

During commissioning observations in 2011, the remote stations produced bad signals in many observations or times. Because of that, we need to get a compromise between keeping the information from remote stations in order to improve the resolution of the image or removing their data to obtain in the end a better calibrated data set (with a lower noise level). Finally, we have used the information of baselines up to  $20\text{ k}\lambda$ , obtaining a synthesized beam of  $15.4 \times 10.8$  arcsec in Position Angle (PA) of 49 degrees (using only the core stations the synthesized beam increases up to  $2.5 \times 1.6$  arcmin in PA of 175 degrees,  $\sim 10$  times poorer resolution).

For practical reasons (to reduce the data volume) we averaged all the data by time intervals of 15 s, and the calibration was done over every subband separately, due to computational cost, i.e. every subband was flagged and calibrated independently from the others. Only during the cleaning process all subbands were combined to produce the final image.

For the calibration process, we have used the LOFAR Standard Imaging Pipeline, which was under development during this time. The pipeline (which is being developed for the LOFAR usage and it is based on `casacore`, the core of the CASA software) consists in a few tasks that we can run in order to reduce the data. The principal tasks are:

**AOFlagger** It is the task to flag the RFI signals from the data. Normally it is run automatically during the averaging stage of the data (after the correlation of the multiple signals). The frequency range observed by LOFAR is considerably affected by RFI, so an efficient task to remove this interferences is essential to obtain good images. Therefore, this process is essential in LOFAR observations.

**Demixing** This procedure removes from the observation data set the interferences caused by the strongest radio sources from the sky. In special the A-team (Cygnus A, Cas A, Vir A, etc). For the LBAs it is essential to calibrate properly the target source and for HBAs it can improve the results. It is applied to all LBA (and sometimes HBA) observations. For the data reduction of our observation it was not used.

**NDPPP** (the New Default Pre-Processing Pipeline) It is the data preprocessing routine to perform the flagging and averaging of the data. The NDPPP is used to clean the data set to be ready to perform the calibration.

**BBS** (BlackBoard Selfcal) It is the task to calibrate or simulate the LOFAR data. This is the main process in the LOFAR Standard Imaging Pipeline, and the process which takes the largest amount of time. After the BBS run, we already have one calibrated data set.

**AWImager** It is the task designed to perform the imaging of the data. Currently it is under a heavy development.

Although almost all the RFI signals are automatically flagged by the AOFlogger system, for our observation we also required an intensive inspection and flagging over some baselines and antennas. Some of them had a strange behaviour during the observation (large amplitudes with a high variability). When the bad antennas are identified, this information is used by the NDPPP task in order to flag automatically these antennas through all sub bands.

For the calibration we need a model of that region of the sky. We built this sky model with the NVSS (NRAO VLA Sky Survey) data (Condon et al. 1998). The cleaning process was made with the `clean` task of CASA instead of the AWImager of the Standard Imaging Pipeline. As the AWImager is under a heavy developing stage, it is not optimized and for the complete data set of our observation it required a prohibitive computational cost, with several programming bugs. In contrast, the CASA task is more stable and produces the image faster.

## Results

With these data we have obtained the image shown in Figure 4.1. The rms (*root mean square*) of the image is  $11 \text{ mJy beam}^{-1}$ . At a distance of  $\sim 10$  arcmin from LS 5039 we are able to detect two bright radio sources with a peak flux density of  $\sim 2.6 \text{ Jy beam}^{-1}$  for the brighter one (the south-eastern one). Other weaker sources are also visible in the full image. At the LS 5039 position we do not detect any signal above the image noise, placing a 3-sigma upper limit of  $33 \text{ mJy beam}^{-1}$ .

## 4.2. Low Frequency VLA Observations

There are two low frequency VLA observations of LS 5039 (project code AM877), with so far unpublished results. These observations consists of two runs: the first one from December 15, 2006 at 22:34 to December 16, 2006 at 00:33, with a total on-source observation time of 80 minutes; the second one from December 17, 2006 at 23:25 to December 18, 2006 at 01:25, with a total on-source observation time of 60 minutes. The post-periastron phases of LS 5039 were 0.5 and 0.0, respectively. These observations were conducted at 330 MHz with the VLA system in C configuration. For the calibration process, Cygnus A, 0137+331 and 1822-096 were observed.

### Data Reduction

These VLA data required a hard flagging process in order to remove all the bad data. The data had several problems. First, the elevation of the source was less than 30 degrees

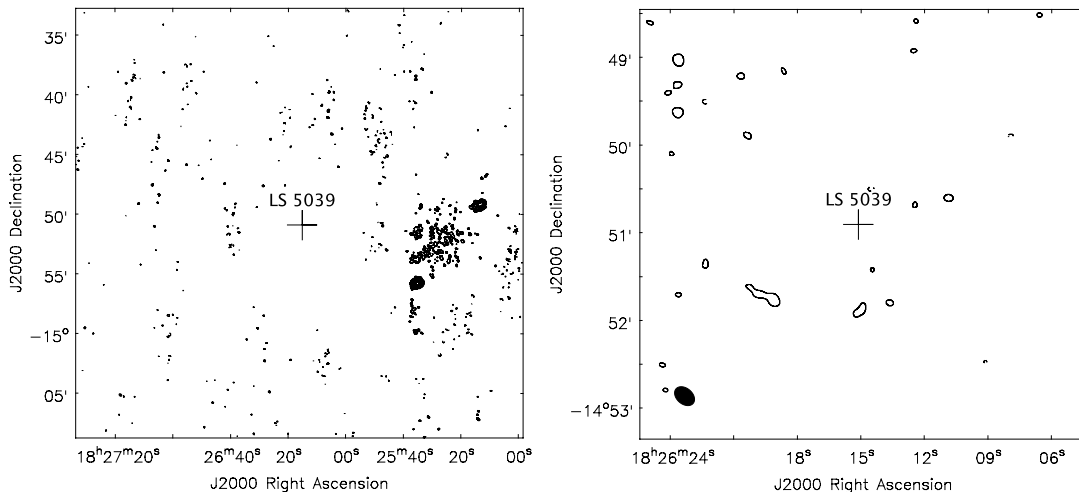


**Figure 4.1.** **Left:**  $40 \times 40$  arcmin image of the field around LS 5039 obtained with LOFAR at frequencies 110–160 MHz on October 1, 2001 during a 6-hour run. The primary beam is  $\sim 5$  degrees and the synthesized beam is  $15.4 \times 10.8$  arcsec in Position Angle of 49 degrees. It is shown in the bottom-left corner of each image (not visible in the left one). The rms of the image is  $11 \text{ mJy beam}^{-1}$  and the contours start at  $3\text{-}\sigma$  noise level, and increase by factors of  $\sqrt{2}$ . **Right:** zoom of the left image displaying  $5 \times 5$  arcmin field, with contours start at  $2\text{-}\sigma$  noise level and increase by factors of  $\sqrt{2}$ . No signal from the position of LS 5039 is detected.

above the horizon during all the observation time (even less than 10 degrees during all the second-night observation). The lower elevation causes bigger ionospheric interferences such as fluctuations in the position of the source, in the amplitudes and in the phases of the received signal, scintillation or a larger value of the noise. Because of that, the signal from the source with an elevation  $\lesssim 15$  degrees was flagged, elevation at which the visibilities showed visible amplitude fluctuations.

Second, there were two problems as a consequence of the elevation of the source and the compact C configuration of the array: shadowing and cross-talk problems. The shadowing problem is originated when a low-elevation source is observed with a compact configuration of the array. In these cases, part of the dish of some antennas is hidden by another antenna as seen from the source, i.e. the source is not seen by the whole dish of every antenna, only by part of it. The JVLA team strongly recommends that all data from a shadowed antenna be discarded, therefore we flagged all the data from a few antennas that suffered from this effect. The cross-talk is a classical problem which the VLA has had with the low frequency receivers. It is an effect in which signals from one antenna are picked up by a close antenna, causing a failed correlation. We think this effect was visible for many baselines which were also completely removed from the final data. Also RFI, usually seen at these low frequencies, were removed from the data.

The calibration was made using the CASA software, Cygnus A was used for the amplitude calibration and Cygnus A and 1822–096 were used for the phase calibration.



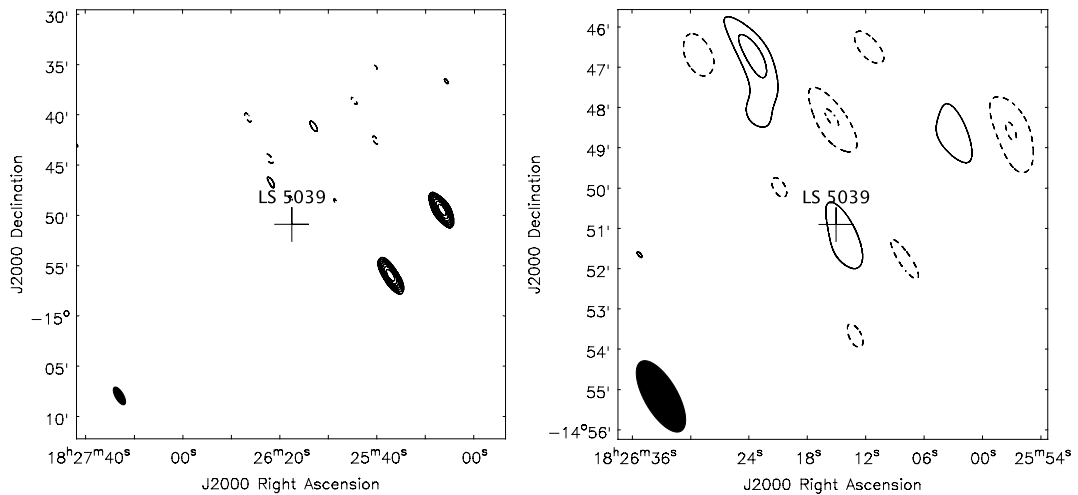


**Figure 4.2.** **Left:**  $42 \times 42$  arcmin image of the field around LS 5039 obtained with the low frequency VLA observation at 330 MHz taken from December 15, 2006 at 22:34 to December 16, 2006 at 00:33 with a unflagged on-source observation time of  $\sim 60$  minutes. The primary beam is  $\sim 2.3$  degrees and the synthesized beam (shown in the bottom-left corner) is  $1.99 \times 0.82$  arcmin in position angle of 32 degrees. The rms of the image is  $42 \text{ mJy beam}^{-1}$ , and the contours start at  $3\text{-}\sigma$  noise level and increase by factors of  $\sqrt{2}$ . **Right:** zoom of the left image displaying  $10 \times 10$  arcmin field, with contours start at  $2\text{-}\sigma$  noise level, and increase by factors of  $\sqrt{2}$ . We only obtain a  $\sim 2\text{-}\sigma$  marginal detection of LS 5039.

We used Cygnus A instead of 0137+331 because of the larger flux density of the first one. Being brighter, the amplitudes and phases of Cygnus A along the time are more stable than for the other sources, and the calibration reported better results with it. A phase self-calibration was made on the image using the detection of two bright nearby sources in order to improve the phases and get an image with a lower rms.

## Results

For these data we have obtained the image shown in the Figure 4.2. The synthesized beam is  $1.99 \times 0.82$  arcmin in position angle of 32 degrees and the rms of the image is  $42 \text{ mJy beam}^{-1}$ . Close to the LS 5039 position (at a distance  $\sim 10$  arcmin) we are able to detect the two radio sources with a flux density of  $\sim 1 \text{ Jy beam}^{-1}$  also detected in the LOFAR data (see Figure 4.1).

At LS 5039 position we only obtain a marginal detection around  $2\text{-}\sigma$  noise level. The flux density inside the  $1\text{-}\sigma$  contour around LS 5039 position is  $108 \text{ mJy beam}^{-1}$ . In any case, this high rms noise level does not allow us to conclude if this signal indeed comes from the emission of LS 5039 or it is just noise.

### 4.3. VLA monitoring

In contrast to the previous observations, we have also worked with higher frequency observations taken with the VLA from September 23, 2002 to October 21, 2002 (project code AP444) during 16 runs. All these data remained unpublished. These runs cover almost the entire orbit of LS 5039, with a time-on-source in each run between 20 minutes and 1 hour. The observations were taken at 1.4, 5.0, 8.5 and 15 GHz (20, 6, 3.5 and 2 cm, respectively), with a BC or C VLA configuration. 1331+305 was used as flux calibrator, and 1834–126 (at 1.4 GHz), 1820–254 (at 5.0 and 8.5 GHz) and 1911–201 (at 15 GHz) were used as phase calibrators.

#### Data Reduction

The calibration at these frequencies is easier because the effects of the ionosphere (important at low frequencies) or the troposphere (important at very high frequencies) are smaller and there are less external interferences than at low frequencies. Therefore the final signal provided by the VLA antennas is more stable than at other frequencies. All the observations were reduced with the CASA software. In all the observations a self-calibration was made. Only for the 15 GHz band the self-calibration was more complicated to carry out because the LS 5039 flux density is weaker at this frequency, and without a bright source on the field, the self-calibration requires a better data to work properly.

#### Results

In all the images LS 5039 is clearly detected. Moreover, for all frequencies except 1.4 GHz, LS 5039 is the only source in the field of view. At 1.4 GHz we also see the two radio sources mentioned for the previous observations, but in this occasion close to the limit of the field of view. The synthesized beam is  $14''$ ,  $5.3''$ ,  $2.5''$  and  $1.4''$ , for 1.4 GHz, 5.0 GHz, 8.5 GHz and 15 GHz, respectively, and the mean rms for the images are 1.7, 0.39, 0.35 and  $0.48 \text{ mJy beam}^{-1}$ . At any orbital phase and any frequency, LS 5039 appears as a point-like source. That is, no morphological features are shown at arcsecond scales.

In Figure 4.3 we show a sample of the images obtained for these observations, and in Figure 4.4 we can see the flux density of LS 5039 as a function of its orbital phase at every observed frequency. It is clear that there is no orbital modulation in the flux density, although a variability  $\sim 20\%$  is observed in week timescales.

Focusing on the dependence of the flux density as a function of the frequency range, we can see that for all orbital phases the flux density exhibit approximately a power-law function, with a slightly flatness at the lower frequencies. For this reason we show in the Figure 4.5 the evolution of the spectral index divided in two frequency intervals: from 1.4 to 5.0 GHz and from 5.0 to 15 GHz. In this way we are able to see that for the lower range the spectral index is generally larger ( $\sim -0.35$ ) whereas in the higher range the spectral index is  $\sim -0.5$ . The spectral index is also variable, but we can not detect any orbital periodicity.

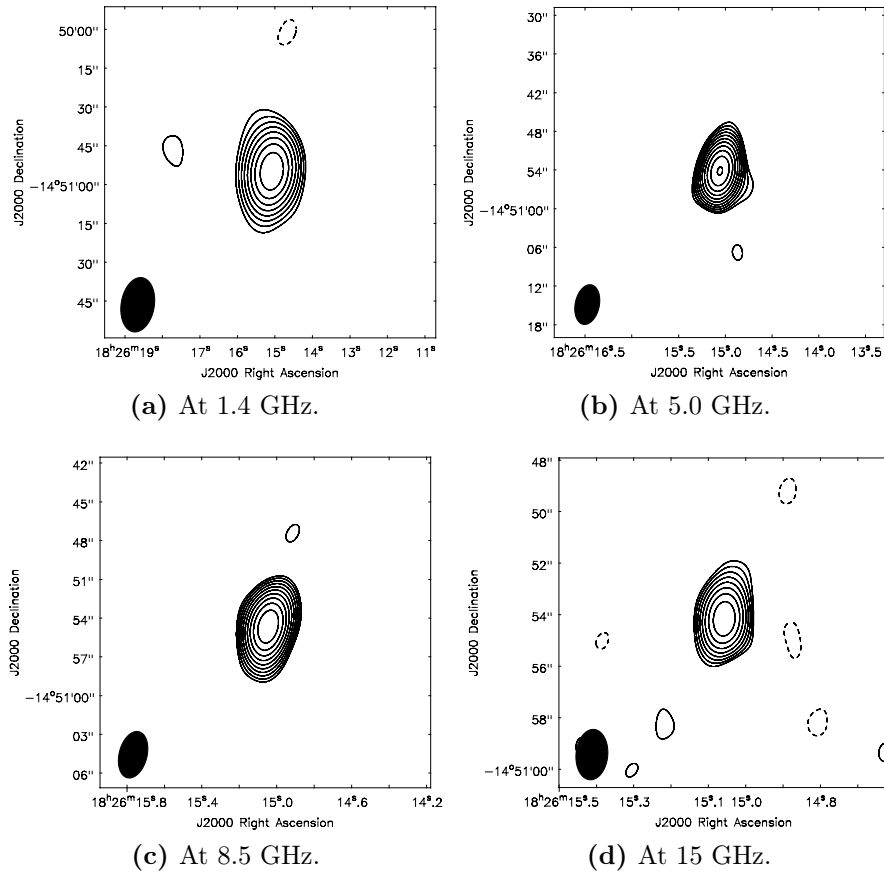


**Figure 4.3.** A sample of the images of LS 5039 obtained with the VLA during the monitoring from September 23, 2002 to October 21, 2002. In all cases LS 5039 appears as a point-like source. The contours start at a  $3\text{-}\sigma$  noise level and increase by factors of  $\sqrt{2}$ . The synthesized beam is shown in the bottom left corner of each image.

#### 4.4. Low frequency variability of LS 5039

We started knowing that LS 5039 exhibits persistent, variable ( $\sim 30\%$ ) flux density at  $\sim$ GHz frequencies whereas at lower frequencies it is possible to show a larger variability ( $\sim 80\%$ ) at about year or less timescales. Combining all the available data up to now, and waiting for all the GMRT data, we are able to conclude that there are strong evidences of the variability of LS 5039 at low frequencies as we can infer from the Figure 4.6. The LOFAR upper limit indicates without doubt that at low frequencies there is an absorption which produces a positive spectral index. This upper limit is in addition compatible with the report of Godambe et al. (2008) but it requires the presence of a strong absorption (with a spectral index steeper than  $\alpha = -2.5$ ) between 150 – 230 MHz to be compatible with the Pandey et al. (2007) results. Therefore, some kind of large variability with, at least, year timescales seems to be required to be able to explain all these observations in the range of 150–600 MHz.

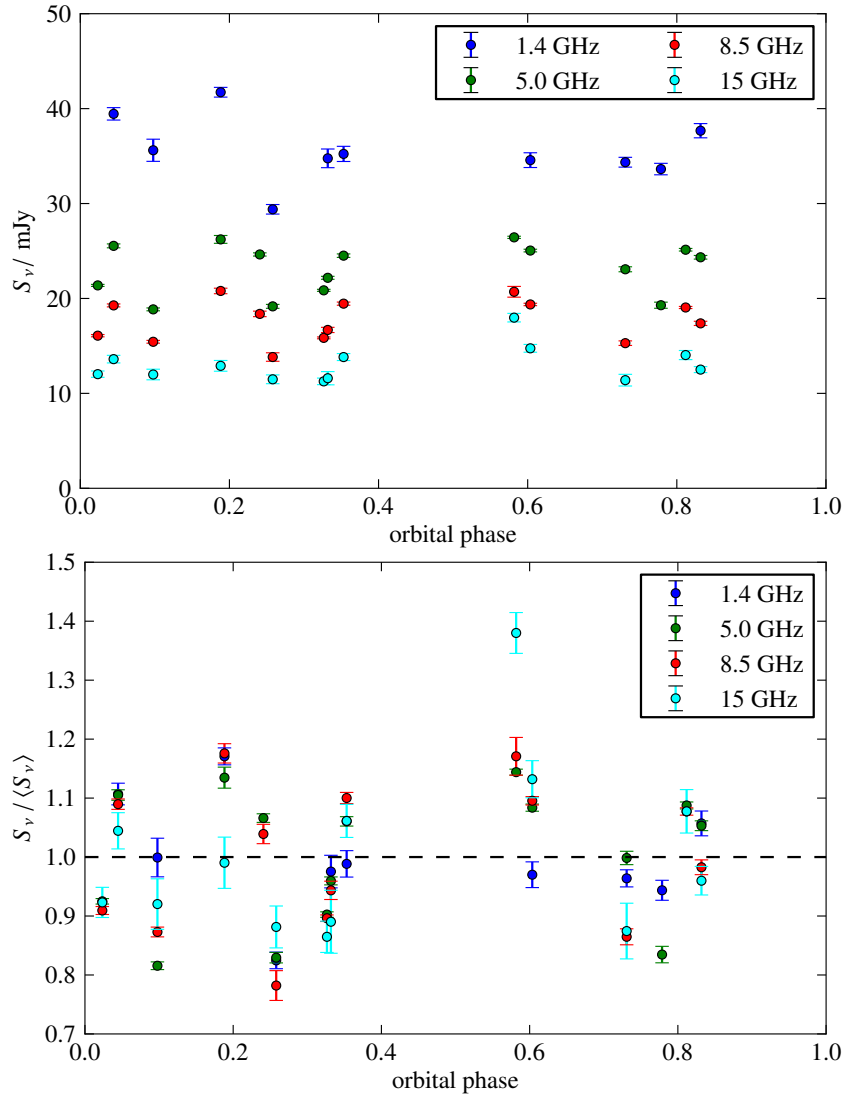


**Figure 4.4.** (top) Evolution of the flux density of LS 5039 as a function of the orbital phase for each observed frequency. (bottom) Ratio between the flux density at each observation and the mean flux density at each frequency (the mean value for all observations taken along the orbit for each frequency). The variability is clearly seen at all frequencies, but does not show any orbital modulation.

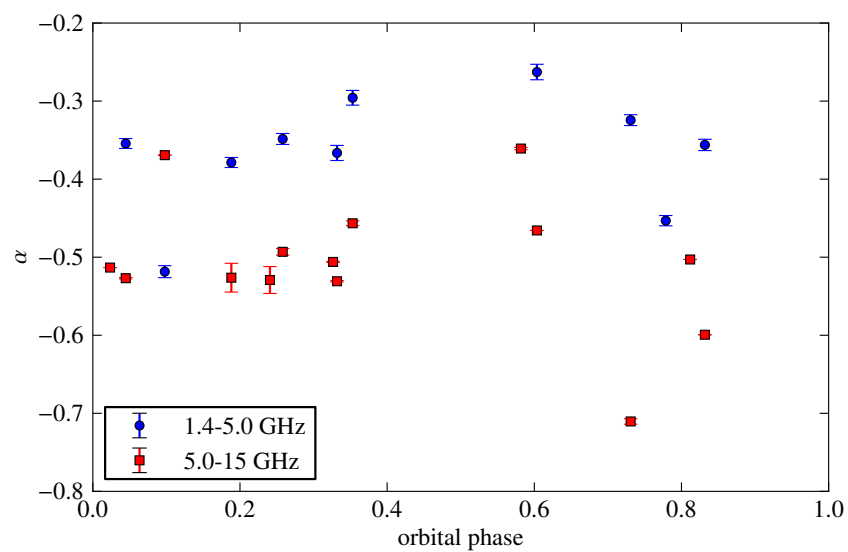


**Figure 4.5.** Evolution of the spectral index of LS 5039 as a function of the orbital phase for two regions of the spectra: from 1.4–5.0 GHz (blue circles) and for 5.0–15 GHz (red squares). For the first range the mean spectral index is  $\alpha = -0.362 \pm 0.004$  whereas in the higher range  $\alpha = -0.51 \pm 0.02$ . Variability in both spectral indexes is seen, but we can not confirm if there is an orbital modulation.

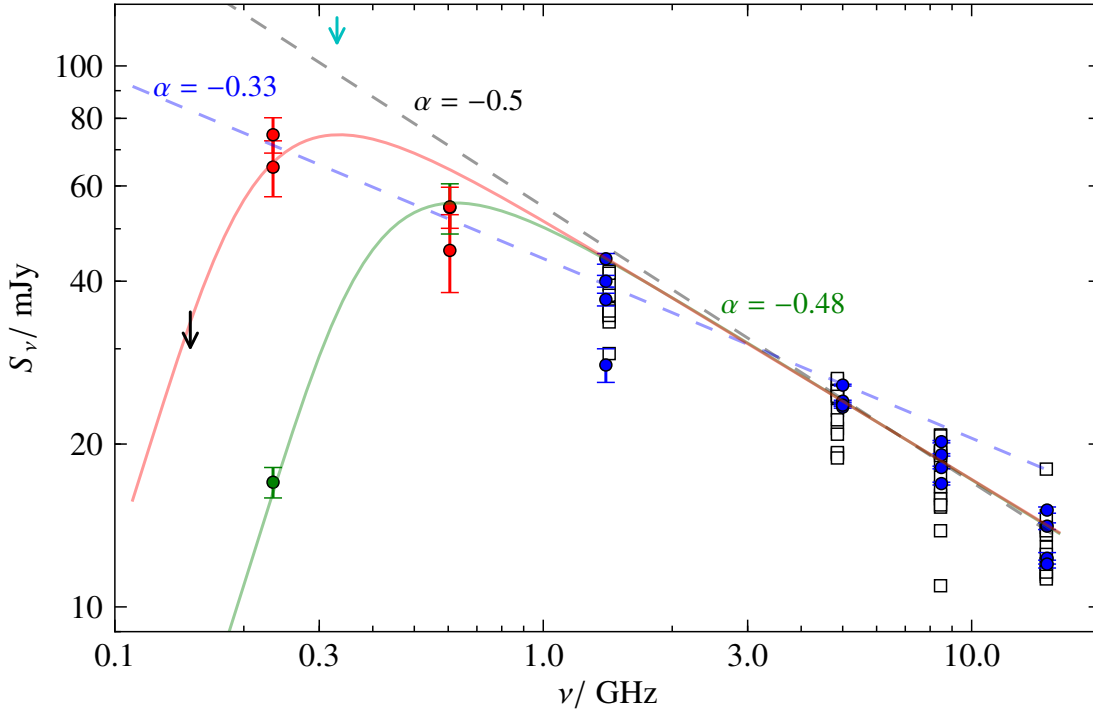


**Figure 4.6.** Flux density of LS 5039 as a function of the frequency for all available observations. The observations at  $\sim$ GHz frequencies are from [Martí et al. \(1998\)](#) (blue points) and from the VLA monitoring (white squares), the red points are the observations of [Pandey et al. \(2007\)](#) with GMRT, the green ones (at 230 and 610 MHz) are from [Godambe et al. \(2008\)](#), the cyan arrow is the  $3\text{-}\sigma$  upper limit from the low frequency VLA observation and the black arrow is the  $3\text{-}\sigma$  upper-limit from the LOFAR observation. All the data were taken at different epochs and the error bars show the  $1\text{-}\sigma$  error for each measure. The 610 MHz results published here have been corrected from the Galactic emission (Ishwara-Chandra, private communication). The dashed lines show the expected synchrotron emission without absorption for the spectral index obtained at high frequencies (gray dashed line) or a low frequencies (blue dashed line). The solid lines consider the synchrotron self-absorption and are fitted for the [Godambe et al. \(2008\)](#) data (green solid line) or for the [Pandey et al. \(2007\)](#) data plus the LOFAR upper limit (red solid line). The LOFAR upper limit is compatible with the Godambe interpretation of the existence of a cut-off at  $\sim 1$  GHz. Whereas the low frequency VLA detection can not clarify the possible existence of that cut-off. This picture points out a large variability for the low frequency emission of LS 5039, that contrasts with the small variability at frequencies larger than 600 MHz.

Before our study, we only knew that a possible variability at low frequencies for LS 5039 could happen. With the addition of the newly reduced observations more evidences of this variability with at least  $\sim$ year timescales have been added. This behaviour does not happen at high frequencies, at which only a small variability is reported. With the VLA monitoring and comparing it with the other archival observations such as [Martí et al. \(1998\)](#), we can conclude that there is no variability above 30 % at different epochs, and that there is no orbital periodicity in the range of 1.4–15 GHz. At 614 MHz the behaviour of LS 5039 seems to be the same: only a small variability above 30 %, whereas at frequencies lower than 600 MHz there is a large variability, up to  $\sim$  80% in 3 years.

Given that the low frequency emission should be emitted from the larger scale structures of the system, a better determination of the timescales of the low frequency variability will provide us new limits for the scale of these structures and the variations of the physical conditions in them. If this variability obeys to shorter timescales (at this moment we only have upper limits of about years, but we can not conclude anything about orbital periodical changes), some reinterpretation about the emitter region of the binary system should be taken into account in the theoretical models. For now, the origin of this large variability at low frequencies without large variability at high frequencies remains unknown.

This large variability could be produced by a dynamical change in the frequency at which the cut-off takes place. In addition, with more simultaneous data at low frequencies we will be able to distinguish between the different absorption processes which could be happening in LS 5039. In principle the synchrotron self-absorption is the most probable absorption for these systems, and as we can see in the [Figure 4.6](#) it provides a good fit for the [Godambe et al. \(2008\)](#) results. However, if we want to compare the [Pandey et al. \(2007\)](#) results with the LOFAR upper limit, a steeper absorption with a cut-off at  $\sim$  200 MHz would be required.

In the future we are focusing to improve this scenario with the addition of more observations at different epochs but also along consecutive orbits. This will be performed with new radio observations at low frequencies but also with the GMRT archival data of LS 5039, which remains unpublished up to now.

The origin of this low frequency emission, if it comes from the core or from an extended region around the LS 5039, will require deep observations with the two only observatories which have enough resolution: GMRT (if the extended region is larger than  $\sim$  20 arcsec) or LOFAR.





---

## Bibliography

---

- Aharonian, F., Akhperjanian, A. G., Aye, K.-M., et al. 2005, *Science*, 309, 746
- Aharonian, F., Akhperjanian, A. G., Bazer-Bachi, A. R., et al. 2006, *A&A*, 460, 743
- Albert, J., Aliu, E., Anderhub, H., et al. 2007, *ApJ*, 665, L51
- Bosch-Ramon, V., & Barkov, M. V. 2011, *A&A*, 535, A20
- Bosch-Ramon, V., & Khangulyan, D. 2009, *International Journal of Modern Physics D*, 18, 347
- Bosch-Ramon, V., Paredes, J. M., Ribó, M., et al. 2005, *ApJ*, 628, 388
- Casares, J., Ribó, M., Ribas, I., et al. 2005, *MNRAS*, 364, 899
- Condon, J. J., Cotton, W. D., Greisen, E. W., et al. 1998, *AJ*, 115, 1693
- Dubus, G. 2006, *A&A*, 456, 801
- Durant, M., Kargaltsev, O., Pavlov, G. G., Chang, C., & Garmire, G. P. 2011, *ApJ*, 735, 58
- Fender, R. P., Belloni, T. M., & Gallo, E. 2004, *MNRAS*, 355, 1105
- Fermi LAT Collaboration, Abdo, A. A., Ackermann, M., et al. 2009, *Science*, 326, 1512
- Giacconi, R., Gursky, H., Paolini, F. R., & Rossi, B. B. 1962, *Physical Review Letters*, 9, 439
- Godambe, S., Bhattacharyya, S., Bhatt, N., & Choudhury, M. 2008, *MNRAS*, 390, L43
- Heald, G., Bell, M. R., Horneffer, A., et al. 2011, *Journal of Astrophysics and Astronomy*, 32, 589
- Kirk, J. G., Ball, L., & Skjaeraasen, O. 1999, *Astroparticle Physics*, 10, 31
- Kishishita, T., Tanaka, T., Uchiyama, Y., & Takahashi, T. 2009, *ApJ*, 697, L1
- Lewin, W. H. G., & van der Klis, M. 2006, *Compact stellar X-ray sources* (Cambridge University Press)
- Maraschi, L., & Treves, A. 1981, *MNRAS*, 194, 1P
- Martí, J., Paredes, J. M., & Ribó, M. 1998, *A&A*, 338, L71

- McSwain, M. V., Ray, P. S., Ransom, S. M., et al. 2011, *ApJ*, 738, 105
- Moldón, J. 2012, PhD thesis, Universitat de Barcelona
- Moldón, J., Ribó, M., & Paredes, J. M. 2012b, *A&A*, submitted
- Moldón, J., Ribó, M., Paredes, J. M., et al. 2012a, *A&A*, 543, A26
- Motch, C., Haberl, F., Dennerl, K., Pakull, M., & Janot-Pacheco, E. 1997, *A&A*, 323, 853
- Pandey, M., Rao, A. P., Ishwara-Chandra, C. H., Durouchoux, P., & Manchanda, R. K. 2007, *A&A*, 463, 567
- Paredes, J. M., Martí, J., Ribó, M., & Massi, M. 2000, *Science*, 288, 2340
- Rea, N., Torres, D. F., Caliendo, G. A., et al. 2011, *MNRAS*, 416, 1514
- Reig, P. 2011, *Ap&SS*, 332, 1
- Ribó, M., Paredes, J. M., Moldón, J., Martí, J., & Massi, M. 2008, *A&A*, 481, 17
- Romero, G. E., & Paredes, J. P., eds. 2011, *Introducción a la astrofísica relativista*, 1st edn. (Universitat de Barcelona)
- Sabatini, S., Striani, E., Verrecchia, F., et al. 2010, *The Astronomer's Telegram*, 2715, 1
- Sarty, G. E., Szalai, T., Kiss, L. L., et al. 2011, *MNRAS*, 411, 1293
- Tavani, M., & Arons, J. 1997, *ApJ*, 477, 439
- Tavani, M., Bulgarelli, A., Piano, G., et al. 2009, *Nature*, 462, 620
- Taylor, G. B., Carilli, C. L., & Perley, R. A., eds. 1999, *ASP Conference Series*, Vol. 180, *Synthesis Imaging in Radio Astronomy II*
- Williams, S. J., Gies, D. R., Matson, R. A., et al. 2010, *ApJ*, 723, L93

